Article

Solution chemistry back-contact FTO/hematite interface engineering for efficient photocatalytic water oxidation

Karen Cristina Bedin [a,b], Beatriz Mouriño [a], Ingrid Rodríguez-Gutiérrez [a,b],
João Batista Souza Junior [a], Gabriel Trindade dos Santos [a,c], Jefferson Bettini [a],
Carlos Alberto Rodrigues Costa [a], Lionel Vayssieres [d,*], Flavio Leandro Souza [a,b,#]

[a] The National Nanotechnology Laboratory (LNNANO), Brazilian Center for Research in Energy and Materials (CNPEM), Campinas 13083-970, Brazil
[b] Centro de Ciências Naturais e Humanas (CCNH), Federal University of ABC (UFABC), Santo André 09210580, Brazil
[c] Federal University of Rio Grande do Sul (UFRGS), Rio Grande do Sul, Brazil
[d] International Research Center for Renewable Energy (IRCRE), State Key Laboratory of Multiphase Flow in Power Engineering, School of Energy and Power Engineering, Xi'an Jiaotong University, Xi'an 710049, Shaanxi, China

ARTICLE INFO

ABSTRACT

This work describes a simple yet powerful scalable solution chemistry strategy to create back-contact rich interfaces between substrates such as commercial transparent conducting fluorine-doped tin oxide coated glass (FTO) and photoactive thin films such as hematite for low-cost water oxidation reaction. High-resolution electron microscopy (SEM, TEM, STEM), atomic force microscopy (AFM), elemental chemical mapping (EELS, EDS) and photoelectrochemical (PEC) investigations reveal that the mechanical stress, lattice mismatch, electron energy barrier, and voids between FTO and hematite at the back-contact interface as well as short-circuit and detrimental reaction between FTO and the electrolyte can be alleviated by engineering the chemical composition of the precursor solutions, thus increasing the overall efficiency of these low-cost photoanodes for water oxidation reaction for a clean and sustainable generation of hydrogen from PEC water-splitting. These findings are of significant importance to improve the charge collection efficiency by minimizing electron-hole recombination observed at back-contact interfaces and grain boundaries in mesoporous electrodes, thus improving the overall efficiency and scalability of low-cost PEC water splitting devices.

1. Introduction

Over the past several decades, the quest for designing efficient and stable photoelectrodes for clean hydrogen generation from water splitting to facilitate the necessary urgent transition to a low-carbon society has been very challenging for scientists and engineers [1–4]. Moreover, developing cost-effective and large-scale fabrication techniques to produce them safely and reproducibly add up to the strenuous challenge [5–7]. Among several low-cost, tunable and scalable solution chemistry-based

methods [8–11], those derived from the Pechini process do stand out in academic research as well as in industrial processes [12–15]. The benefits of these methodologies include the ease of execution and reproduction, the simple experimental apparatus, the excellent stoichiometric control and versatile design of materials in various forms such as powders, thin films and polymers compared to other methods [12,13]. Regardless of these obvious advantages, scaling up from laboratory to industry and manufacturing large area thin films electrodes for a wide range of optoelectronic applications remain a challenge [16,17].

Of particular interest is the large-scale fabrication of electrodes for photovoltaics and photoelectrochemical (PEC) applications such as solar cells and water splitting for instance where a transparent conductive substrate such as commercial fluorine-doped tin oxide coated glass substrate (FTO) is commonly used in most academic studies [18–20]. FTOs have an irregular surface roughness, over which precursor solutions are deposited by spin- or dip-coating techniques followed by a crucial step, i.e. the thermal treatment, which eliminates the organic content promoting the formation of the inorganic phase with a given morphology and desired crystalline phase. Hence, the conformal feature over the irregular FTO surface is often lost after annealing, resulting in poor thin film adhesion and significant lattice strains [16,17], which affect photogenerated electron/hole transport and thus reduces overall electrode performance. The release of the mechanical stress during the thermal treatment is directly related to the physical and chemical interface mismatches between FTO and the photoactive thin film and is primarily responsible for the creation of a "dead layer" at the back-contact interface. Moreover surface cracks, pinholes and voids severely impair the optoelectronics performance and long-term stability of photoelectrodes [21–23].

An additional problem associated with the stress release is the shunting in the mesoporous photocatalyst morphology, which increases the electron loss due to the FTO exposition to the electrolyte during the thin film application. Although the thin films prepared from polymeric precursor solution are more susceptible to the stress at the substrate/semiconductor interface favoring a creation of shunting recombination pathway, this undesirable aspect is commonly reported for mesoporous morphology regardless of the fabrication process. Several methods devoted to mitigate the shunting recombination in mesoporous thin films, which occurs during the thin film fabrication have been reported in the literature in an attempt to improve photoelectrode performances [24,25]. Among those methods, the deposition of a thin oxide layer (< 15 nm) onto FTO prior to the growth of the desired photoactive layer is the most common strategy [21,23,25]. Indeed, overcoming the shunting recombination issue without compromising the thin film morphology and/or the improvements achieved by modifications is not an easy task. Recently, Hamann [25] proposed an electrodeposition of an insulating poly(phenylene oxide, PPO) layer over the FTO substrate before the photocatalyst deposition. Cyclic voltammetry data showed that indeed the PPO layer can be employed to reduce the shunting recombination at the back contact interface and enhance the hematite

photoanode performance depending on the morphology. Considering that the feasibility to manufacture mesoporous morphology, thermal treatment, and "green" principles are needed for industrial scale-up and cost minimization, fabrication methods that use fewer manufacturing steps are preferable.

In this regard, the hands-on knowledge accumulated by our group throughout the last decade [16,17,26–28], aiming at generally improving interfaces and minimizing/simplifying fabrication steps reached a significant landmark recently [27]. The reduction of water content after obtaining the polymeric precursor solution enabled more effective viscous control allowing the deposition of multiple layers of hematite with superior performance [27]. An additional modification was carried out to obtain similar performance, but synthesizing a monolayer of hematite processed in a single step [28]. By simply modifying the viscosity of the polymeric precursor solution, a single spin-coating deposition allowed a reduction in the number of hematite-hematite interfaces in thin films up to 130 nm in thickness. However, the back-contact FTO-hematite interface was still not optimized, weakening the electronic transport and photoelectrochemical efficiency. A non-conductive tetravalent cation (Sn^{4+}) together with a well-known water oxidation cocatalyst (FeNi) was introduced leading to the formation of a highly mesoporous morphology and increased efficiency [28], yet still far from commercial benchmark expectations, mostly due to interfacial and shunting problems discussed above.

It has long been experimentally observed that photocatalysts performance diverge substantially from their theoretical benchmark efficiency. Although, several advanced characterization tools such as *in situ*/operando techniques [24] were developed to probe interfacial issues, a lack of studies remains in literature regarding critical steps in thin film design and interface control, especially for back-contact interfaces.

The goal of this study was to develop simple chemical modifications of the precursor solutions to engineer the back-contact FTO-photocatalyst interface to improve overall efficiency by reducing a number of critical known issues such as back-contact short-circuit/competing reactions with the electrolyte, photogenerated carriers losses by recombination and high energy barrier, thin film long-term mechanical stability (i.e. avoid peel-off due to electrolyte infiltration in voids), thin film density optimization just to name a few. Hematite was selected as a model system due its extensive interest in the literature for application as photoanodes in PEC cell for water oxidation.

To achieve this goal, the polymeric precursor solution was concentrated at 70 °C and solubilized in a mixture of alcohols together with Zr^{4+} addition. Among the most common tetravalent cations (Sn, Ti) used for boosting hematite performance, Zr^{4+} ions were deliberately chosen due to their relatively low solubility in iron oxide solid solution (compared to Ti for instance which led to the formation of multiple iron titanate phases) and high stability as +IV oxidation state. Although Sn^{4+} has similar characteristics, its presence within the FTO combined with its well-known uncontrolled diffusion during thermal treatment could increase the difficulty in identifying the role and origin of element addition/doping. A full multi-scale

morphological characterization was carried out combining microscopic and nanoscale analysis unveiling the formation of a more suitable back-contact interface employing a low-cost and easily-scalable process to engineer this important yet often neglected interface.

2. Experimental

2.1. Preparation of Zr-hematite thin films

In a typical synthesis, 7.00 g of iron(III) nitrate ($Fe(NO_3)_3 \cdot 9H_2O$, Alfa Aesar, 99.5%) and 10.00 g of citric acid ($C_6H_8O_7$, J.T. Baker, 99.5%) were dissolved in 20 g of milli-Q water (18.2 MΩ cm, 25 °C). The system was then heated at 60–70 °C and kept under stirring throughout the process. After complete homogenization, 6.70 g of ethylene glycol (Sigma Aldrich, 99.8%) was added to this solution, further stirred and heated at 70 °C for 30 min. In this step, the ferric ions are chelated by citric acid and the polyesterification reaction promoted by ethylene glycol occurs. Thereafter, the polymeric precursor solution was allowed to naturally cool down to 25 °C. An aliquot of 10.0 mL was concentrated at 70 °C by reduction of 50% of its initial volume (to 5.0 mL), as illustrated in Fig. 1. At this point, a desired amount of 0.14 mol/L $ZrO(NO_3)_2 \cdot 2H_2O$ (Alfa-Aesar, 99.9%) water-ethanol stock solution (50:50, *v:v*) was added to the iron polymeric solution to obtain the Zr-modified hematite precursor solutions, which were stirred for 5 min. Aliquots of the Zr^{4+}-stock solution were used to obtain the precursor solution with 1%, 2%, 3% and 4% Zr^{4+} in relation to iron (calculated from the stoichiometric reaction of oxides formation), resulting in the ZrH1%, ZrH2%, ZrH3% and ZrH4% thin films, respectively. Five minutes after the Zr^{4+} addition, at 25 °C, 1.50 mL of anhydrous ethanol (Synth, 99.8%) and 1.00 mL of isopropyl alcohol (Synth, 99.5%) were, in this order, slowly added to the solution, which was maintained under stirring for ~15 min. A solution without Zr^{4+} addition was prepared following the same steps to obtain pristine hematite (H) sample. All the solutions were stored in a refrigerator (*T* = 7 °C) for 24 h and all thin film depositions were made at 25 °C with the precursor solutions subjected to stirring prior deposition.

The FTO substrates utilized in this study are commercialized by Solaronix. The conductive layer (SnO_2:F, fluorine doped tin oxide, resistivity of 8 ohm/cm) is deposited over an aluminum borosilicate glass (ABS, 1 mm thick) which enables to sus-

tain relatively higher temperature (∼ 800 °C) for a short period of time without causing serious damage to the substrate conductivity, transparency and structural integrity. The glass composition and FTO thickness around 500 nm were also chosen to strongly limit element diffusion to the photocatalyst layer during thermal treatment. FTO substrates were cleaned by immersion in boiling water-Extran® solution for 30 min, then immediately rinsed and maintained for 15 min in hot water, followed by ethanol and acetone rinsing for 15 min each. The substrates were posteriorly thermal treated in air, at 550 °C for 60 min. A single deposition (50 μL) of the precursor solution was spin coated (5 s at 500 rpm and 30 s at 7000 rpm) onto cleaned and treated substrates. After coating, the thin films were dried for 5 min at 90 °C on a hot plate, and treated for 30 min in Air at 550 °C and for 30 min in N_2 at 750 °C. These chosen temperatures are well-established in the literature to eliminate organic compounds, and crystallize the hematite phase while preserving the substrate [19,20,27].

2.2. Morphology and Interface Characterization

Morphological features were investigated by scanning electron microscopy (SEM) using a Quanta™ FEG 650, FEI Company, in a cross-sectional configuration (30°), with an ETD detector, a high accelerating voltage of 5–7 kV and a spot of 2.0. Working distances were kept between 7–10 mm and the horizontal field width was kept at 3.00 μm. Surface roughness was evaluated by atomic force microscopy (AFM), NX-10 Park Systems in the intermittent contact mode Modo (tapping mode) with silicon probe Nano World, FMR model, Resonance Frequency (nominal) 75 kHz, Force Constant (nominal) 2.8 N/m. Scanning image area of 2 × 2 micrometer with a resolution of 512 × 512 pixels was recorded. RMS average values were determined with Gwyddion Software. Transmission electron microscopy (TEM) analysis was performed on a JEOL JEM 2100F equipped with energy dispersive spectroscopy (EDS), Oxford SDD X-Max 80 mm², and electron energy loss spectroscopy (EELS), Gatan GIF Tridiem 863. Both EDS and EELS data were acquired simultaneously using a 0.7 nm probe size and a 0.1 s time acquisition.

2.3. Photoelectrochemical experiments

Pristine and Zr-modified hematite thin films were tested as photoanodes for water oxidation reaction in a three-electrode electrochemical cell, with a platinum electrode as the counter electrode, commercial (Metrohm Autolab) $Ag/AgCl_{(sat)}$ electrode as the reference electrode and 1.0 mol L^{-1} NaOH (pH 13.6) as the electrolyte solution. The linear sweep voltammograms (LSV) measurements were conducted using a potentiostat/galvanostat (Autolab PGSTAT129N) and sunlight illumination (100 mW cm^{-2}) simulated by a 450 W Xe lamp (Osram, ozone free) equipped with an AM 1.5 global filter with a scan rate of 10 mV s^{-1}. All potentials were converted to the reversible hydrogen electrode (RHE) using the Nernst equation (1):

$$E_{RHE} = E_{Ag/AgCl} + E^0_{Ag/AgCl} + 0.059\text{pH} \qquad (1)$$

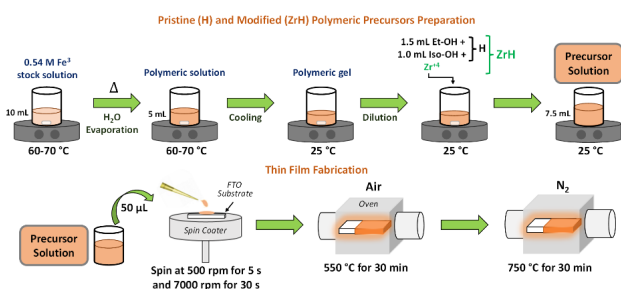Photoelectrodeposition of FeNi cocatalyst onto ZrH3% was

Fig. 1. Schematic representation of the polymeric precursor solution preparation and thin films fabrication process for pristine and Zr-modified hematite photoelectrodes.

performed from its immersion in the electrochemical cell containing an aqueous solution (pH = 5.3) of 16.0 mmol/L Ni-SO$_4$·6H$_2$O (Neon, 100%), 5.0 mmol/L Fe$_2$(SO$_4$)$_3$·H$_2$O (Sigma Aldrich, 97%) and 0.1 mol/L NaCH$_3$COO (Neon, 99.3%). A Platinum wire and commercial (Metrohm Autolab) Ag/AgCl$_{(sat)}$ were used as counter and reference electrodes, respectively. LSV were carried out three times in this system, from 0.5 to 0.9 V *vs.* Ag/AgCl using a scan rate of 10 mV s^{-1}. After this procedure, ZrH3% thin film coated with FeNi (ZrH3%/FeNi) was rinsed with water and no additional treatment was employed.

2.4. Electrochemical impedance spectroscopy experiments

Electrochemical impedance measurements (EIS) were performed using the same three-electrodes configuration cell and electrolyte conditions (1.0 mol L^{-1} NaOH (pH = 13.6). To extract key operational information the EIS data were analyzed by using the Mott-Schottky (M-S) plot. Taking into account the morphology of the thin films and other assumptions reported for a correct application of M-S theory [29], the donor charge density (N_D) for pristine-H and ZrH samples were calculated from the M-S plots recorded at 1 kHz under dark condition, by relating the fitting from the linear regime of the M-S plots and the Eq. (2):

$$N_D = (2/e_0\varepsilon\varepsilon_0) \times (1/slope) \qquad (2)$$

where e_0 is the electron elementary charge (1.60 × 10^{-19} C), ε is the dielectric constant of the semiconductor (80 to hematite), ε_0 is vacuum permittivity (8.85 × 10^{-12} F m^{-1}).

3. Results and discussion

Chemical-based route was employed to design pristine hematite and optimized to afford different concentration of Zr^{4+} addition as shown in Fig. 1. After, spin-coating deposition of the polymeric precursor solution and thermal treatment step the obtained thin films were named as pristine-H (H-hematite) and ZrH(x%) according to the Zr concentration (x = 1 wt%, 2 wt%, 3 wt%, and 4 wt%). The quality of the FTO coverage and thin film morphology were monitored by scanning electron and atomic force microscopies (Figs. S1 and S2). A full coverage of FTO (Fig. S1(a)) and good thin film adhesion can be observed in the fracture view of SEM images for all compositions (Fig. S1). Apparently, no significant change in morphology is observed from SEM analysis upon Zr^{4+} addition, maintaining a typical elongated grain shape usually referred to as wormlike [16,17,30]. However, the surface roughness significantly decreases with increasing Zr^{4+} concentration in the precursor solution. From the topographic AFM images (Fig. S2), surface roughness values were estimated and summarized in Table S1 showing a substantial decrease from 26 for FTO to 6.0 and 5.0 RMS for pristine-H and ZrH(x%) thin films, respectively.

The cross-sectional view of designed hematite highlights the bottleneck of the chemical-based process (Fig. 2), which is associated with few regions of oxide layer in contact with the irregular morphology of the commercial FTO substrate. In our previous work [28], a solvent exchange during the final stage of precursor solution preparation enabled a monolayer deposi-
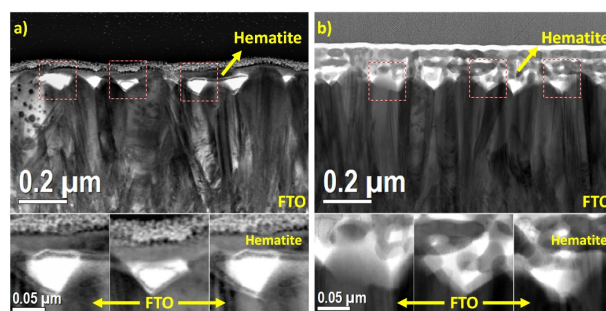

Fig. 2. STEM images of hematite single solvent (a) and mixing solvent (b) and Zr^{4+} addition layers. Bottom: Magnified regions represented by red squares highlighting the contrast of poor and rich contact between photocatalyst thin film and commercial FTO glass substrate.

tion as shown in Fig. 2(a). Although this result allows a successful control of the film thickness from 15 to 130 nm in a single deposition, the contact between photocatalyst monolayer and the FTO is unlikely to yield an efficient charge transport. The evidence of poor interface is well represented by the magnified regions of the highlighted red squares in the scanning transmission electron microscopy (STEM) images (Fig. 2(a)).

The current strategy adopted a combination of an adequate ratio between ethanol/isopropanol solvent and Zr^{4+} concentration that enabled stable precursor solution, homogenous thin film deposition favoring a new morphology formation that increased the back-contact interface that so far consisting of empty regions (voids). The highlighted red squares regions in Fig. 2(b) (bottom STEM images) revealed contact-rich regions between photocatalyst and the FTO. Interestingly, the thin film deposition followed the same previous spin coating condition with fixed amount of solution and subsequent thermal treatment. STEM images of pristine-H and ZrH thin films corroborate with the surface roughness reduction discussed above Fig. S2, in which the layer grows filling the FTO valleys until the formation of a smooth and relatively flat layer on top.

A plausible explanation to obtain completely different thin film morphology, as revealed above, can be linked to the specificities of the polymeric precursor solution preparation. By looking at the schematic diagram in Fig. 1, the polymeric precursor solution is concentrated by reducing its initial volume until a polymeric gel consistence. Then, an optimized ratio of solvents mixture (ethanol/isopropanol) was used at 25 °C to solubilize the viscous polymeric gel. So, the solubilized polymeric gel may have assumed a different conformation favoring a more suitable molecular packing on FTO surface during the thermal treatment as illustrated in Fig. 3. Two factors lead to the new morphology observed, one related to the faster elimination of the well-packed polymeric solution and the other due to the Zr^{4+} addition. Indeed, the Zr^{4+} presence at the oxide surface induces an energy drop alleviating the competition between hematite grain growth and the stress at the FTO-layer interface (Fig. 3, bottom) during the thermal treatment.

Further in-depth high-resolution insights at the back-contact FTO-photocatalyst interface were carried out in pristine-H and ZrH thin films by high resolution transmission electron microscopy (HRTEM). Representative interfaces are
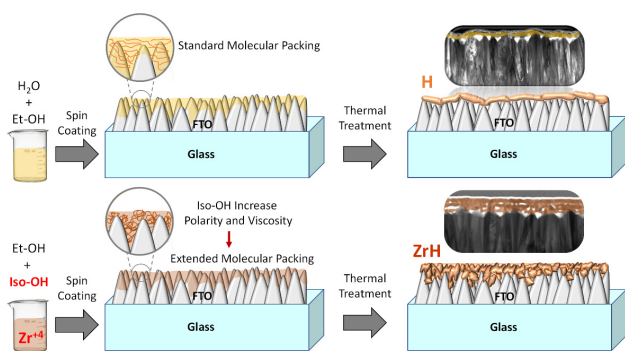
Fig. 3. Schematic representation of the different molecular configurations leading to better contact interface between FTO and photocatalyst during thermal treatment. More suitable molecular packing along with the Zr^{4+} segregation at hematite surface is providing an appropriate environment for the growth of a back-contact-rich interface.

displayed in Fig. 4 showing the HRTEM images for the interface region (white squares Figs. 4(a) and 4(f)) and their surroundings. Interplanar distances and lattice mismatch for FTO (SnO_2:F)/pristine-H and FTO/ZrH at the interfaces (white squares in Figs. 4(b) and 4(g)) were calculated and summarized in Tables S1–4. The mismatch between epitaxial plane of growth of pristine-H and ZrH on FTO were also measured considering several similar interfaces. As a result, the average mismatch for the pristine-H was $(3.8 \pm 1.6)\%$, and for the ZrH was $(1.7 \pm 0.9)\%$. The highest mismatch for the pristine-H was 6.3% [$(111)/(\bar{2}1\bar{2})$], as represented in Figs. 4(a)–(e), while for the ZrH was 3.8%. The results strongly indicate that the FTO-pristine-H interfaces are submitted to stronger stress during the thermal treatment, which may partially explain why hematite growth only on top of the FTO crystal (Fig. 2(a) and Fig. 4(a)). Comparing experimental interplanar distances of FTO (not at the interface but within the surrounding area with
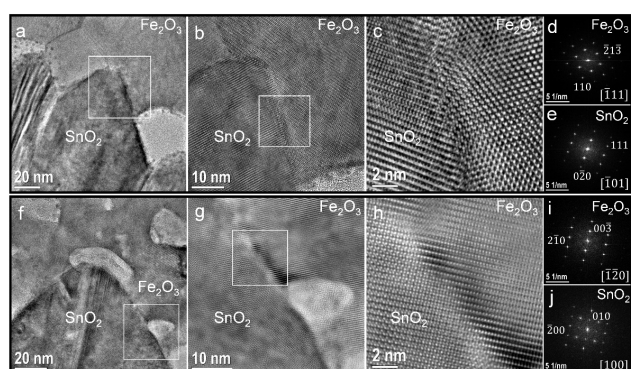

Fig. 4. TEM images of pristine hematite/FTO interface showing (a) low magnification image and HRTEM images at two different magnifications for (b) the tip of FTO/hematite interface (white box in image a) and (c) filtered HRTEM of lateral FTO (SnO_2)/hematite interface (white box in image d; (e,f) Fast Fourier Transform (FFT) images of hematite and FTO (SnO_2) regions in image c indexed with the crystallographic planes in green and red dots along with the zone axis in the right side bottom corner of the images. TEM images of FTO/ZrH3% interface (hematite containing Zr) showing (f) low magnification image and HRTEM images with two magnifications for (g) the lateral interface and (h) filtered HRTEM of lateral FTO/ZrH3% interface (white box in image h), (i,j) FFT images of hematite (α-Fe_2O_3) and FTO (SnO_2) regions in image h.

the standard SnO_2, rutile structure $P4_2/mnm$ (ICSD-90611) the average mismatch corroborates by showing higher distortion for pristine-H (Table S3). Similarly, the average mismatch comparing experimental interplanar distances for hematite at the surroundings with the standard hematite (α-Fe_2O_3, ICSD-7799, $R\bar{3}c$) for both pristine-H and ZrH shows distortion (Table S4 and Fig. 4) probably influenced by the crystal growth at the rough FTO surface. The slightly higher mismatch exhibited by ZrH can be related to the presence of Zr^{4+}. Herein, the mismatch evidenced by the HRTEM study at FTO-photocatalyst interface has also been discussed in the literature among several issues preventing high performance [31–34].

To further investigate the experimental implication of the developed approach to design efficient photoelectrodes, electrochemical experiments were conducted simulating half of a PEC cell. $J \times V$ curves displayed in Fig. 5(a) show that the photocurrent response of pristine-H thin film (solid black line) gradually improves (from 0.53 mA cm^{-2} at 1.23 V_{RHE}) with Zr^{4+} addition, achieving the maximum efficiency with 3% of Zr (ZrH3%, green solid line) around 1.2 mA cm^{-2} at 1.23 V_{RHE}. Further addition of Zr^{4+} led to a reduction in performance (> 0.9 mA cm^{-2} at 1.23 V_{RHE}, orange solid line, Fig. 5(a)).

Concomitant with the improvement in performance, a slight anodic shift in the onset potential was observed comparing pristine H with ZrH thin films (from 0.88 to 0.95 V_{RHE}). In literature, the addition of elements such as Sn [35–37], Ti [38–40] and Sb [41,42] that preferentially segregate at the hematite surfaces (e.g., surface exposed to the electrolyte) instead of doping has been associated with the appearance of surface states and observed onset potential anodic shift. Herein, a similar behavior was attributed to Zr^{4+} addition. Usually, elements that tend to segregate at hematite crystal surface led to three major distinct effects (1) pinning the grain growth by dropping the surface energy at the grain boundaries, which also has positive impact in the charge transport through the hematite grain, [37,43] (2) creating surface states at the exposed surface to the liquid leading to changes in the flat band potential position, and (3) less common effective doping of hematite by increasing the donor density (N_D). Since (1) and (2) have already been attributed to Zr^{4+} addition in previous discussion, further investigations were performed to probe possible doping (3).

To clarify the interfacial charge separation as well as transfer process, EIS and photoelectrochemical impedance spectroscopy (pEIS) measurements were performed for all the samples. The discussion was concentrated in the HZr3%/FeNi photoelectrode that exhibit superior performance and compared with its pristine-H form. As observed in the Nyquist plots under illumination (Fig. 6(a)), the pEIS spectra are composed by two mixed depressed semicircles and adequately fitted with an equivalent circuit (Fig. 6(a), inset) consisting of resistors and capacitors (electrolyte resistance (R_s), bulk resistance (R_s), bulk capacitance (C_{bulk}), the charge transfer resistance (R_{ct}), and a constant phase element (CPE) associated with the surface states capacitance (C_{ss})) which highlights the role of the surface states and the bulk contribution in the photoelectrochemical process.

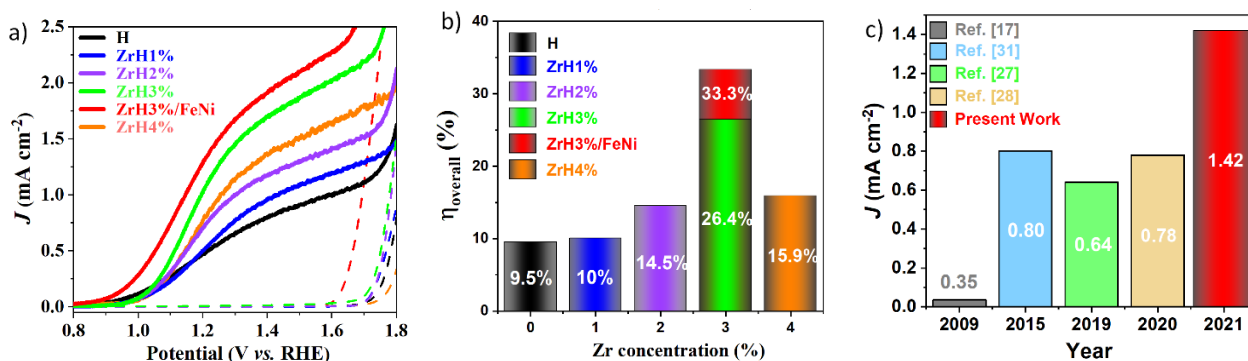Table 1 summarizes the fitting parameters of R_s, R_{bulk}, C_{bulk},

Fig. 5. (a) Linear sweep voltammograms of pristine hematite, ZrH1%, ZrH2%, ZrH3% and ZrH4% measured in 1.0 mol/L NaOH at scan rate of 10 mV s^{-1}. The solid lines represent the response under AM 1.5G illumination (100 mW cm^{-2}) and the dashed lines under dark conditions, and (b) Overall efficiency ($\eta_{overall}$) obtained for the ratio J_{ph}/J_{abs} for all the prepared thin films, (c) Photocurrent densities extracted at 1.23 V (RHE) from literature using the same chemical procedure method and similar planar thin film morphology showing a Si^{4+}-doped (black line, —) [17], Cu^{2+}-doped (blue line, —) [31], pristine Hematite multiple layers (green line, —) [27], Sn^{4+}-doped/FeNi (orange line, —) [28], and the ZrH3%/FeNi (present work, red line, —). The reported photocurrent densities were measured in 1.0 mol/L NaOH aqueous solution at pH = 13.6.

R_{ct}, and CPE. It is noticeable that the ZrH3%/FeNi photoanode exhibited remarkably decreased resistances in both bulk (197.1 W) and charge transfer resistance (21.5 W) when compared with H photoanode (540 and 361.9 W respectively), confirming the minimization of electron losses due to Zr^{4+} segregation and the facilitated interface charge transfer between the ZrH3%/FeNi and the electrolyte.

Moreover, the EIS data were analyzed in terms of Mott-Schottky plot to extract the values of N_D for all hematite thin films produced in the current investigation. The estimated values of 5.03×10^{-19} cm^{-3} for pristine hematite and 2.39×10^{-20} (ZrH1%), 4.60×10^{-20} (ZrH2%) and 5.34×10^{-20} cm^{-3} (ZrH3%) demonstrate an effective Zr doping by the enrichment of donor charge density (N_D) of one order of magnitude (Eq. S(1) and Fig. 6(b)). Interestingly, the developed approach favored a combination of these three effects improving the electronic properties (N_D) and leading to the formation of a new

morphology (segregating at the grain boundary).

To avoid any misinterpretation, overall efficiencies ($\eta_{overall}$) were determined for the thin films normalizing the photocurrent response by the optical features related to their microstructural parameter. $\eta_{overall}$ is obtained from the ratio J_{ph}/J_{abs}, in which J_{abs} represents the upper limit of photocurrent density as a function of the electrode absorbance efficiency (see supporting information for further details). The estimated value of J_{abs} was obtained from the integration of the UV-Vis spectrum of each photoelectrodes (Fig. S3), representing the photocurrent related to its absorption properties, according to the literature [44,45]. The dimensionless quantity ($\eta_{overall}$) confirms that the ZrH3% photoelectrode is nearly three times more efficient than the pristine one and twice higher comparing to other Zr concentration (Fig. 5(b)). Thus, ZrH3% sample was selected for additional scrutiny and improvement. A compelling next step towards better efficiency would be to passivate the surface,
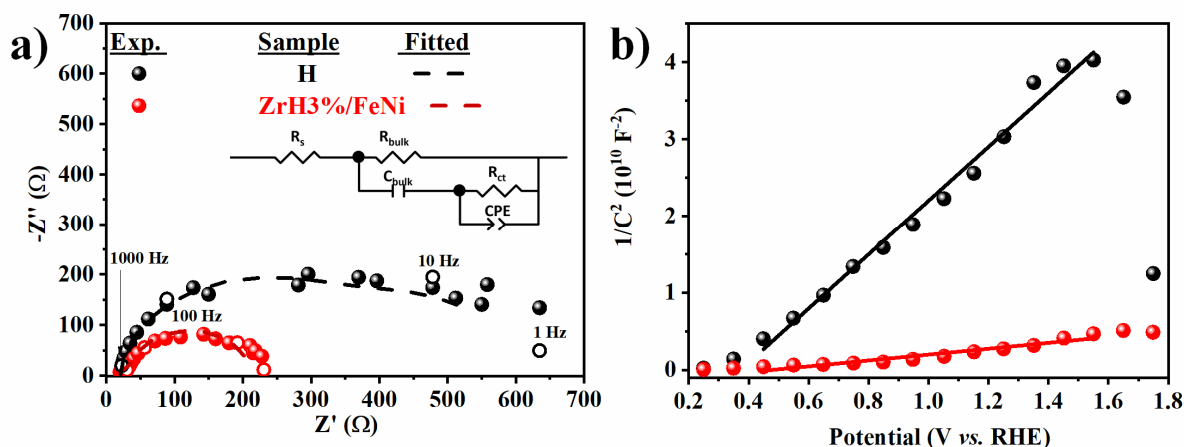

Fig. 6. (a) EIS spectra for pristine-H (black line, —) and ZrH3%/FeNi (red line, —) measured at 1.23 V *vs.* RHE under illuminated conditions; the dashed lines represent the fitting curves obtained from the equivalent circuit inserted in a). (b) Mott-Schottky plots recorded at 1 kHz in dark condition for Pristine-H and ZrH3%/FeNi. Solid lines represent the linear fit to the selected experimental data. The experiment was measured in 1.0 mol/L NaOH solution at pH = 13.6.

Table 1
Fitting parameters derived from the photoelectrochemical Impedance Spectroscopy of H and ZrH3%/FeNi photoanodes at 1.23 V (V *vs.* RHE).

photoanode	R_s (W)	R_{bulk} (W)	C_{bulk} (F)	R_{ss} (W)	CPE_{ss} (F)
H	20.04	540	1.86E-05	361.9	2.73E-05
ZrH3%/FeNi	14.01	197.1	2.11E-05	21.51	1.52E-05

which can be done by adding a cocatalyst at the top surface for increased photogenerated hole injection through the electrolyte [46–48].

Therefore, following a well-established strategy from the literature [49], a typical FeNi cocatalyst was photoelectrodeposited on top of the surface. The adopted strategy led to a shift to lower onset potential (0.8 V_{RHE}) comparing to all other electrodes, including the pristine hematite. This cathodic shift is a fingerprint of surface state passivation by FeNi addition, which improves $\eta_{overall}$ photoelectrochemical performance without causing significant changes on the optical and microstructural properties [49–51]. Operando characterization techniques have been employed for in-depth understanding of the role played by FeNi as an overlayer at the photocatalyst-electrolyte interface [50]. It has been shown that most of the holes photogenerated at the hematite migrates to the Ni atoms in the overlayer (being stored prior to promoting the water oxidation reaction) [50]. Including ZrH3%/FeNi photoanode performance in the $\eta_{overall}$ plot (Fig. 5(b)), the overall efficiency increased 7% compared to the ZrH3%. The photocurrent values achieved here with thin films thickness around 100 nm were superior in comparison with other "planar" hematite photoanodes produced by similar methodologies as illustrated in Fig. 5(c). It is worth mentioning that the Zr^{4+} addition was not exclusive to the present work as several reports in the literature have also shown that zirconium has a great potential for improving hematite performance regardless of morphology and synthetic methods [52–56].

Further analyses were conducted to exploit the morphological and physical-chemical properties of ZrH3%/FeNi combining SEM/AFM and HRTEM/EELS/EDS.

SEM cross-sectional view shown in Fig. 7 follows the fabrication step for pristine (a to b) and ZrH3%/FeNi (a-c-d) showing no apparent change in morphology. The addition of FeNi is
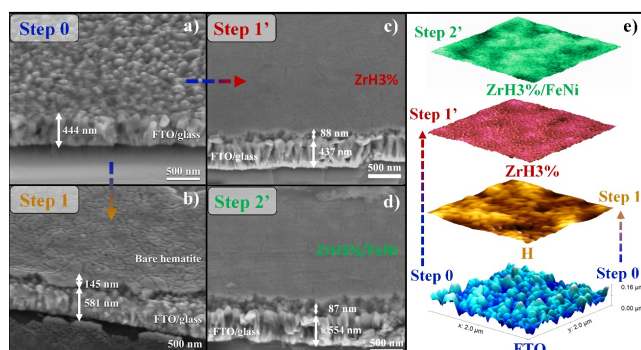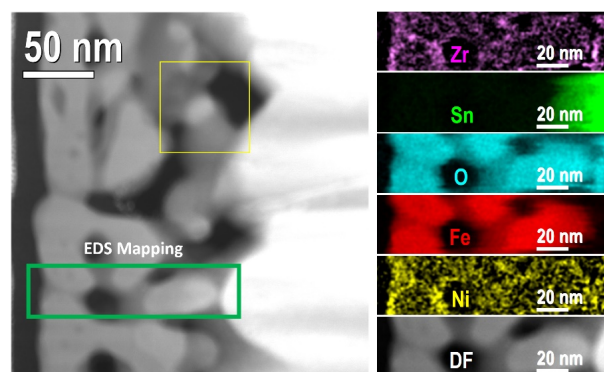

Fig. 8. STEM image and chemical mapping images obtained from EDS for the ZrH3%/FeNi thin film. The area marked with a yellow box was used to drift correction and the green box is the mapping region.

expected not to alter the morphology since no additional thermal treatment is required [49,51,57]. However, the surface roughness drastically changes from 26 (FTO) to 5 RMS (ZrH3%/FeNi), values even lower than pristine hematite, forming a smooth surface. Indeed, after FeNi deposition, the FTO rough topography can no longer be observed (Fig. 7(e)).

The chemical composition of the ZrH3%/FeNi thin film was determined by EDS analysis during STEM image acquisitions. A representative back-contact FTO-ZrH3%/FeNi interface region (green box, Fig. 8) was analyzed and shows that the chemical composition reveals the Sn-rich (green) at FTO area, the hematite photocatalyst (red), Oxygen (blue) well distributed throughout all the materials (oxide phases), Ni (yellow) spread over the iron surface and Zr preferably segregated at the hematite crystals interface (purple color, Fig. 8).

EELS analysis revealed that the iron (hematite) chemical environment changes around the back-contact FTO/Hematite interface and at the top Hematite surface as seen in Fig. 9. To better understand this process, an EELS color mapping showing the energy shift from standard Fe^{+3} $L_{2,3}$ edge (ΔeV) was plotted. The contrasting colors denote a variation on chemical oxidation state or disturbance in the chemical bond, due to
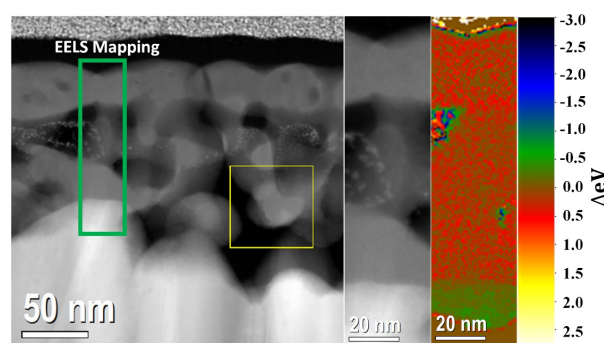

Fig. 7. Cross-section SEM images for FTO (a), pristine hematite (b), ZrH3% (c), ZrH3%/FeNi (d) and their corresponding AFM topographical images (e).

Fig. 9. STEM image and STEM/EELS energy shift mapping (ΔeV) for L_3-edge of Fe in the rectangular green box. Variations of oxidation state and chemical environment of iron are displayed by the ΔeV color map where differences from the brown color (ΔeV equal 0) represents differences from the standard L_3-edge peak position for iron in hematite. The square yellow box was used for drift correction in the STEM/EELS mapping.
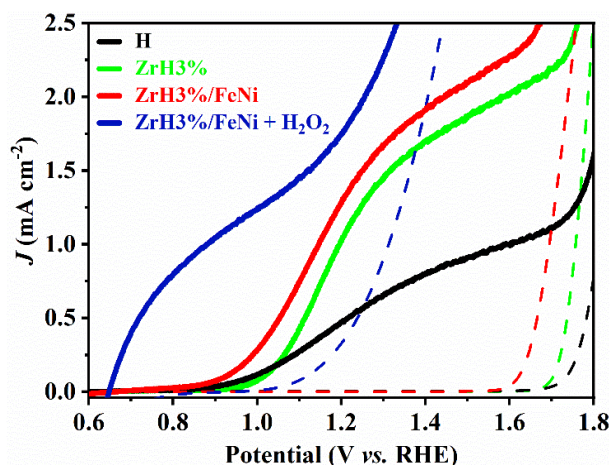
Fig. 10. Linear sweep voltammograms of pristine-H, ZrH3% and ZrH3%/FeNi measured in 1.0 mol/L NaOH + 5% H_2O_2 for ZrH3%/FeNi at scan rate of 10 mV s^{-1}. The solid lines represent the response under AM 1.5G illumination (100 mW cm^{-2}) and the dashed lines under dark conditions.
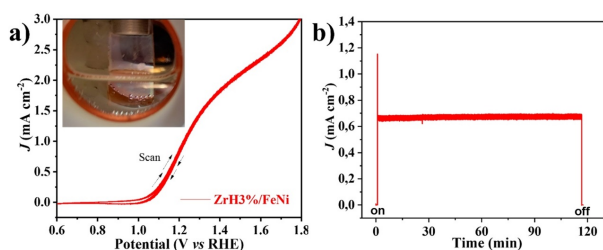

Fig. 11. (a) Cyclic voltammetry of ZrH3%/FeNi photoanode up to 200 scans from 0.6 to 1.8 V *vs.* RHE under simulated light conditions (forward scan and 50 mV/s scan rate and light intensity calibrated at 100 mW; (b) Chronoamperometry curve of ZrH3%/FeNi at 1.23 V *vs.* RHE.

interactions of atoms with their adjacent ones, causing a shift in energy in these areas [58]. Among the two distinct contrasting regions, the first located at the FTO/Hematite interface (green region with blue shift in energy and ΔeV of –0.5 eV) indicates that the epitaxial growth of hematite over FTO leads to tin diffusion of few angstroms towards the hematite lattice. The second region, located on the top surface of hematite thin film (green to blue contrast color, ΔeV of –0.5 to –2.0 eV), shows the presence of the iron content in the thin layer of FeNi, which is revealed by the Fe^{+3} $L_{2,3}$ edge shift (blue region, ΔeV > –2.0 eV) originated from the chemical bound of Fe-Ni. FeNi preferential segregation on top of hematite surface was expected due to the adopted deposition method. The EELS color mapping result also corroborates what was concluded on the distribution of the elements in the EDS analysis (Fig. 8), which showed that Zr cations do not significantly diffuse into the bulk hematite. The other two contrast regions are explained by the holes in the hematite thin film seen in the STEM image, i.e. the absence of iron on those two regions creates the color difference that do not contain significant information.

Herein, the recorded data from nano- to micro-scale clearly reveals that the back-contact interface can be efficiently tuned and optimized by simply adjusting the polymeric precursor solution chemistry. Thus, the engineered interface may avoid

FTO exposition to electrolyte, mitigating electron loss by recombination and/or competing detrimental reactions as well as short circuit. Further experiments conducted on ZrH3%/FeNi photoanode in the presence of a typical hole scavenger such as hydrogen peroxide (H_2O_2) shows that these back-contact engineered photoanodes could still be further improve in performance (1.9 mA cm^{-2} and an even lower onset potential of 0.65 V_{RHE}) as seen in Fig. 10.

Furthermore, stability tests were conducted to investigate the quality of the ZrH3%/FeNi under simulated operation condition (Fig. 11). Cyclic voltammetry measurements were performed over 200 cycles from 0.6 to 1.5 V_{RHE} (scan rate 50 mV s^{-1}) under illuminated conditions (Fig. 11(a)). In all cycles, stable J_{ph} and V_{onset} were recorded which reveal good stability of ZrH3%/FeNi in NaOH aqueous electrolyte under applied potential and one-sun illumination. Chronoamperometry measurements (Fig. 11(b)) showed a spike when the light is on, indicating recombination processes at the solid-liquid interface yet the photocurrent density stabilizes within 5 s and remains steady afterwards during a preliminary 2h-test. Long-term performance and stability studies will be investigated in the future.

4. Conclusions

This study presents a simple, yet powerful strategy, manipulating the chemistry of polymeric precursor solutions to successfully fabricate smooth thin film hematite-based photoanodes onto rough and irregular commercial FTO substrates. The as-prepared novel morphology efficiently optimized the back-contact substrate-photocatalyst interface, which led, not only to the minimization of electron losses by recombination commonly observed at grain boundaries in mesoporous electrodes, but as important to better thin film density for optimized optical absorption. The engineered back-contact-rich interface also prevents the detrimental presence of voids which commonly lead to thin film stability failure as well as competing (photo)electrochemical reactions and short-circuit between the substrate and the electrolyte without the presence of an additional buffer layer. High resolution nanoscale chemical composition mapping and electron microscopy analysis of the interfaces by EELS and EDS revealed that the Zr^{4+} preferentially segregated over the hematite interfaces, while FeNi stays located over the exposed surfaces to the electrolyte acting as a cocatalyst. AFM analysis also shows a stronger stress felt by pristine-H in comparison with ZrH photocatalyst, which can explain the better back-contact interface. The developed solution chemistry-based strategy to fabricate and engineer the back-contact interface between substrate and catalyst is definitely not limited to only overcoming current critical issues in photocatalyst and photovoltaic thin films grown on FTO but can surely be easily extended to more industry-friendly substrates such as low-cost stainless steel [59] and electronics-grade silicon wafers [60] for instance as well as other types of electrodes for a wider range of existing applications such as sensors, energy storage and conversion devices and flexible electronics given the low-temperature synthesis fabrication.

Graphical Abstract

Chin. J. Catal., 2022, 43: 1247–1257　　doi: 10.1016/S1872-2067(21)63973-6

Solution chemistry back-contact FTO/hematite interface engineering for efficient photocatalytic water oxidation

Karen Cristina Bedin, Beatriz Mouriño, Ingrid Rodríguez-Gutiérrez, João Batista Souza Junior, Gabriel Trindade dos Santos, Jefferson Bettini, Carlos Alberto Rodrigues Costa, Lionel Vayssieres *, Flavio Leandro Souza *
Brazilian Center for Research in Energy and Materials (CNPEM), Brazil; Federal University of ABC, Brazil; Federal University of Rio Grande do Sul, Brazil; Xi'an Jiaotong University, China
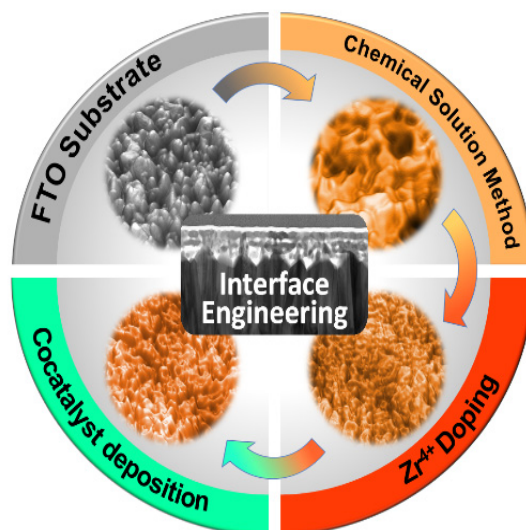
To minimize photogenerated carrier losses and improve overall PEC efficiency, the back-contact FTO-photocatalyst interface is engineered using a simple and scalable solution chemistry process.

Finally, the combination of additional emerging characterization techniques specifically suitable for probing interfaces such as intensity modulated photocurrent spectroscopy (IMPS) [61] as well as element-sensitive in-situ/operando X-ray spectroscopies [62] and X-ray spectro-microscopy [63] now available at several synchrotron radiation facilities worldwide, along with time-resolved spectroscopies [1] and artificial intelligence (AI) and machine learning [65] would certainly enhanced our comprehensive fundamental understanding of the role of all components and reaction mechanisms involved in photo-oxidation of water, an essential and crucial half reaction for the truly clean generation of hydrogen from water and sunlight.

Conflict of interest

There are no conflicts to declare.

Acknowledgments

Electronic supporting information

Supporting information is available in the online version of this article.

References

[1] J. Li, H. Chen, C. A. Triana, G. R. Patzke, *Angew. Chem. Int. Ed.*, **2021**, 60, 18380–18396.

[2] B. Iandolo, B. Wickman, I. Zorić, A. Hellman, *J. Mater. Chem. A*, **2015**, 3, 16896–16912.

[3] K. Sivula, *J. Phys. Chem. Lett.*, **2013**, 4, 1624–1633.

[4] J. Zhang, J. Cui, S. Eslava, *Adv. Energy Mater.*, **2021**, 11, 2003111.

[5] D. Zhou, K. Fan, *Chin. J. Catal.*, **2021**, 42, 904–919.

[6] Z. Wang, L. Wang, *Chin. J. Catal.*, **2018**, 39, 369–378.

[7] F. Li, J. Jian, Y. Xu, S. Wang, H. Wang, H. Wang, *Eng. Reports*, **2021**,

3, e12387.

[8] L. Vayssieres, N. Beermann, S. E. Lindquist, A. Hagfeldt, *Chem. Mater.*, **2001**, 13, 233–235.

[9] L. Vayssieres, M. Graetzel, *Angew. Chem. Int. Ed.*, **2004**, 43, 3666–3670.

[10] R. H. Gonçalves, B. H. R. Lima, E. R. Leite, *J. Am. Chem. Soc.*, **2011**, 133, 6012–6019.

[11] T. Katsuki, Z. N. Zahran, K. Tanaka, T. Eo, E. A. Mohamed, Y. Tsubonouchi, M. R. Berber, M. Yagi, *ACS Appl. Mater. Interfaces*, **2021**, 13, 39282–39290.

[12] A. E. Danks, S. R. Hall, Z. Schnepp, *Mater. Horizons*, **2016**, 3, 91–112.

[13] J. Kang, Y. R. Gwon, S. K. Cho, *J. Electroanal. Chem.*, **2020**, 878, 114601.

[14] M. Kakihana, K. Domen, *MRS Bull.*, **2000**, 25(9), 27–31.

[15] M. Kakihana, M. Yoshimura, H. Mazaki, H. Yasuoka, L. Börjesson, *J. Appl. Phys.*, **1992**, 71, 3904–3910.

[16] F. L. Souza, K. P. Lopes, E. Longo, E. R. Leite, *Phys. Chem. Chem. Phys.*, **2009**, 11, 1215–1219.

[17] F. L. Souza, K. P. Lopes, P. A. P. Nascente, E. R. Leite, *Sol. Energy Mater. Sol. Cells*, **2009**, 93, 362–368.

[18] M. H. Tang, P. Chakthranont, T. F. Jaramillo, *RSC Adv.*, **2017**, 7, 28350–28357.

[19] J. E. N. Swallow, B. A. D. Williamson, T. J. Whittles, M. Birkett, T. J. Featherstone, N. Peng, A. Abbott, M. Farnworth, K. J. Cheetham, P. Warren, D. O. Scanlon, V. R. Dhanak, T. D. Veal, *Adv. Funct. Mater.*, **2018**, 28, 1701900.

[20] J. K. Yang, B. Liang, M. J. Zhao, Y. Gao, F. C. Zhang, H. L. Zhao, *Sci. Rep.*, **2015**, 5, 15001.

[21] L. Steier, I. Herraiz-Cardona, S. Gimenez, F. Fabregat-Santiago, J. Bisquert, S. D. Tilley, M. Grätzel, *Adv. Funct. Mater.*, **2014**, 24, 7681–7688.

[22] Z. Zhou, L. Li, Y. Niu, H. Song, X.-S. Xing, Z. Guo, S. Wu, *Dalton Trans.*, **2021**, 50, 2936–2944.

[23] O. Zandi, B. M. Klahr, T. W. Hamann, *Energy Environ. Sci.*, **2013**, 6, 634–642.

[24] M. R. Nellist, F. A. L. Laskowski, J. Qiu, H. Hajibabaei, K. Sivula, T. W. Hamann, S. W. Boettcher, *Nat. Energy*, **2018**, 3, 46–52.

[25] P. Shadabipour, T. W. Hamann, *Chem. Commun.*, **2020**, 56, 2570–2573.

[26] D. A. Bellido-Aguilar, A. Tofanello, F. L. Souza, L. N. Furini, C. J. L. Constantino, *Thin Solid Films*, **2016**, 604, 28–39.

[27] D. N. F. Muche, T. M. G. dos Santos, G. P. Leite, M. A. Melo, R. V. Gonçalves, F. L. Souza, *Mater. Lett.*, **2019**, 254, 218–221.

[28] D. N. F. Muche, S. A. Carminati, A. F. Nogueira, F. L. Souza, *Sol. Energy Mater. Sol. Cells*, **2020**, 208, 110377.

[29] K. Sivula, *ACS Energy Lett.*, **2021**, 6, 2549–2551.

[30] J. Y. Kim, G. Magesh, D. H. Youn, J.-W. Jang, J. Kubota, K. Domen, J. S. Lee, *Sci. Rep.*, **2013**, 3, 2681.

[31] Y. Li, N. Guijarro, X. Zhang, M. S. Prevot, X. A. Jeanbourquin, K. Sivula, H. Chen, Y. Li, *ACS Appl. Mater. Interfaces*, **2015**, 7, 16999–17007.

[32] Z. Zhang, I. Karimata, H. Nagashima, S. Muto, K. Ohara, K. Sugimoto, T. Tachikawa, *Nat. Commun.*, **2019**, 10, 4832.

[33] H. Zhang, D. Li, W. J. Byun, X. Wang, T. J. Shin, H. Y. Jeong, H. Han, C. Li, J. S. Lee, *Nat. Commun.*, **2020**, 11, 4622.

[34] F. A. L. Laskowski, M. R. Nellist, J. Qiu, S. W. Boettcher, *J. Am. Chem. Soc.*, **2019**, 141, 1394–1405.

[35] L. Xi, S. Y. Chiam, W. F. Mak, P. D. Tran, J. Barber, S. C. J. Loo, L. H. Wong. *Chem. Sci.*, **2013**, 4, 164–169.

[36] J. Wang, N. H. Perry, L. Guo, L. Vayssieres, H. L. Tuller, *ACS Appl. Mater. Interfaces.*, **2019**, 11, 2031–2041.

[37] M. R. S. Soares, C. A. R. Costa, E. M. Lanzoni, J. Bettini, C. A. O. Ramirez, F. L. Souza, E. Longo, E. R. Leite, *Adv. Electron. Mater.*, **2019**, 5, 1900065.

[38] C. X. Kronawitter, I. Zegkinoglou, S. H. Shen, P. Liao, I. S. Cho, O. Zandi, Y. S. Liu, K. Lashgari, G. Westin, J. H. Guo, F. J. Himpsel, E. A. Carter, X. L. Zheng, T. W. Hamann, B. E. Koel, S. S. Mao, L. Vayssieres, *Energy Environ. Sci.*, **2014**, 7, 3100–3121.

[39] T. J. Smart, V. U. Baltazar, M. Chen, B. Yao, K. Mayford, F. Bridges, Y. Li, Y. Ping, *Chem. Mater.*, **2021**, 33, 4390–4398.

[40] B. Scherrer, T. Li, A. Tsyganok, M. Döbeli, B. Gupta, K. D. Malviya, O. Kasian, N. Maman, B. Gault, D. A. Grave, A. Mehlman, I. Visoly-Fisher, D. Raabe, A. Rothschild, *Chem. Mater.*, **2020**, 32, 1031–1040.

[41] A. Annamalai, R. Sandström, E. Gracia-Espino, N. Boulanger, J. F. Boily, I. Mühlbacher, A. Shchukarev, T. Wågberg, *ACS Appl. Mater. Interfaces*, **2018**, 10, 16467–16473.

[42] A. E. Nogueira, M. R. Santos Soares, J. B. Souza Junior, C. A. Ospina Ramirez, F. L. Souza, E. R. Leite, *J. Mater. Chem. A*, **2019**, 7, 16992–16998.

[43] S. C. Warren, K. Voïtchovsky, H. Dotan, C. M. Leroy, M. Cornuz, F. Stellacci, C. Hébert, A. Rothschild, M. Grätzel, *Nat. Mater.*, **2013**, 12, 842–849.

[44] S. M. Thalluri, L. Bai, C. Lv, Z. Huang, X. Hu, L. Liu, *Adv. Sci.*, **2020**, 7, 1902102.

[45] O. Zandi, T. W. Hamann, *Phys. Chem. Chem. Phys.*, **2015**, 17, 22485–22503.

[46] M. R. Nellist, J. Qiu, F. A. L. Laskowski, F. M. Toma, S. W. Boettcher, *ACS Energy Lett.*, **2018**, 3, 2286–2291.

[47] R. Li, C. Li, *Adv. Catal.*, **2017**, 60, 1–57.

[48] J. Yang, D. Wang, H. Han, C. Li, *Acc. Chem. Res.*, **2013**, 46, 1900–1909.

[49] C. G. Morales-Guio, M. T. Mayer, A. Yella, S. D. Tilley, M. Grätzel, X. Hu, *J. Am. Chem. Soc.*, **2015**, 137, 9927–9936.

[50] A. Tsyganok, P. Ghigna, A. Minguzzi, A. Naldoni, V. Murzin, W. Caliebe, A. Rothschild, D. S. Ellis, *Langmuir*, **2020**, 36, 11564–11572.

[51] Q. Xu, H. Jiang, X. Duan, Z. Jiang, Y. Hu, S. W. Boettcher, W. Zhang, S. Guo, C. Li, *Nano Lett.*, **2021**, 21, 492–499.

[52] A. Subramanian, E. Gracia-Espino, A. Annamalai, H. H. Lee, S. Y. Lee, S. H. Choi, J. S. Jang, *Appl. Surf. Sci.*, **2018**, 427, 1203–1212.

[53] S. Shen, P. Guo, D. A. Wheeler, J. Jiang, S. A. Lindley, C. X. Kronawitter, J. Z. Zhang, L. Guo, S. S. Mao, *Nanoscale*, **2013**, 5, 9867–9874.

[54] I. K. Jeong, M. A. Mahadik, J. B. Hwang, W. S. Chae, S. H. Choi, J. S. Jang, *J. Colloid Interface Sci.*, **2021**, 581, 751–763.

[55] C. Li, Z. Luo, T. Wang, J. Gong, *Adv. Mater.*, **2018**, 30, 1707502.

[56] C. Li, A. Li, Z. Luo, J. Zhang, X. Chang, Z. Huang, T. Wang, J. Gong, *Angew. Chem. Int. Ed.*, **2017**, 56, 4150–4155.

[57] A. Tsyganok, D. Klotz, K. D. Malviya, A. Rothschild, D. A. Grave, *ACS Catal.*, **2018**, 8, 2754–2759.

[58] S. Mourdikoudis, R. M. Pallares, N. T. K. Thanh, *Nanoscale*, **2018**, 10, 12871–12934.

[59] Y. Wei, J. Su, L. J. Guo, L. Vayssieres, *Sol. Energy Mater. Sol. Cells*, **2019**, 201, 110083.

[60] X. Guan, F. A. Chowdhury, Y. Wang, N. Pant, S. Vanka, M. L. Trudeau, L. J. Guo, L. Vayssieres, Z. Mi, *ACS Energy Lett.*, **2018**, 3, 2230–2231.

[61] I. Rodriguez-Gutierrez, J. B. Souza Junior, E. R. Leite, L. Vayssieres, F. L. Souza, *Appl. Phys. Lett.*, **2021**, 119, 071602.

[62] C.-L. Dong, L. Vayssieres, *Chem. Eur. J.*, **2018**, 24, 18356–18373.

[63] K. T. Arul, H.-W. Chang, H.-W. Shiu, C.-L. Dong, W.-F. Pong, *J. Phys. D: Appl. Phys.*, **2021**, 54, 343001.

[64] J. B. Souza Jr, F. L. Souza, L. Vayssieres, O. K. Varghese, *Appl. Phys. Lett.*, **2021**, 119, 200501.

[65] H. Masood, C. Y. Toe, W. Y. Teoh, V. Sethu, R. Amal, *ACS Catal.*, **2019**, 9, 11774–11787.

基于溶液化学策略构建背接触**FTO**/赤铁矿光阳极界面工程的高效光催化水氧化研究

Karen Cristina Bedin [a,b], Beatriz Mouriño [a], Ingrid Rodríguez-Gutiérrez [a,b], João Batista Souza Junior [a], Gabriel Trindade dos Santos [a,c], Jefferson Bettini [a], Carlos Alberto Rodrigues Costa [a], Lionel Vayssieres [d,*], Flavio Leandro Souza [a,b,#]

[a]巴西能源和材料研究中心, 国家纳米技术实验室, 坎皮纳斯13083-970, 巴西
[b]ABC联邦大学, 自然和人文科学中心, 圣安德烈, 巴西
[c]南里奥格兰德联邦大学, 南里奥格兰德, 巴西
[d]西安交通大学能源与电力工程学院, 电力工程多相流国家重点实验室, 可再生能源国际研究中心(IRCRE), 陕西西安710049, 中国

摘要: 本文采用一种简单、有效的规模化溶液化学策略, 在基底(如商用氟掺杂氧化锡透明导电涂层玻璃(FTO))和光活性薄膜(如赤铁矿)之间形成丰富的背接触界面, 并用于低成本水氧化反应. 高分辨率电子显微镜(扫描电镜、透射电镜、扫描透射电镜)、原子力显微镜、元素成像(电子能量损失谱和能量色散谱)和光电化学研究表明, 可通过前驱体溶液的化学成分工程来有效降低机械应力、晶格失配、电子势垒和FTO与赤铁矿在背面接触界面之间的空隙以及FTO与电解液之间的短路和有害反应, 进而提升这些低成本光阳极对水氧化反应以及PEC水分解清洁、可持续地生产氢气的整体效率. 本研究对通过最小化在介孔电极的背接触界面和晶粒边界上的电子-空穴复合, 进而提高电荷收集效率具有重要意义, 可提高低成本PEC水裂解装置的整体效率和规模化的能力.

关键词: 纳米结构; 氧化铁; 水氧化; 光阳极; 表面工程; 化学合成